Published in final edited form as:

IEEE Trans Med Imaging. 2016 September ; 35(9): 2085–2097. doi:10.1109/TMI.2016.2549918.

Reconstruction of 7T-Like Images From 3T MRI

Khosro Bahrami [Member, IEEE],
Department of Radiology and BRIC, University of North Carolina at Chapel Hill, Chapel Hill, NC 27514 USA

Feng Shi [Member, IEEE],
Department of Radiology and BRIC, University of North Carolina at Chapel Hill, Chapel Hill, NC 27514 USA

Xiaopeng Zong,
Department of Radiology and BRIC, University of North Carolina at Chapel Hill, Chapel Hill, NC 27514 USA

Hae Won Shin,
Departments of Neurology and Neurosurgery, University of North Carolina at Chapel Hill, Chapel Hill, NC 27514 USA

Hongyu An, and
Department of Radiology and BRIC, University of North Carolina at Chapel Hill, Chapel Hill, NC 27514 USA

Dinggang Shen [Senior Member, IEEE]
Department of Radiology and BRIC, University of North Carolina at Chapel Hill, Chapel Hill, NC 27514 USA

Department of Brain and Cognitive Engineering, Korea University, Seoul, South Korea

Khosro Bahrami: khosrobahrami2010@gmail.com; Feng Shi: fengshi@med.unc.edu; Xiaopeng Zong: xiaopeng_zong@med.unc.edu; Hae Won Shin: shinhw@neurology.unc.edu; Hongyu An: hongyu_an@med.unc.edu; Dinggang Shen: dgshen@med.unc.edu

Abstract

In the recent MRI scanning, ultra-high-field (7T) MR imaging provides higher resolution and better tissue contrast compared to routine 3T MRI, which may help in more accurate and early brain diseases diagnosis. However, currently, 7T MRI scanners are more expensive and less available at clinical and research centers. These motivate us to propose a method for the reconstruction of images close to the quality of 7T MRI, called 7T-like images, from 3T MRI, to improve the quality in terms of resolution and contrast. By doing so, the post-processing tasks, such as tissue segmentation, can be done more accurately and brain tissues details can be seen with higher resolution and contrast. To do this, we have acquired a unique dataset which includes

---

Correspondence to: Dinggang Shen, `dgshen@med.unc.edu`.

This paper has supplementary downloadable material available at http://ieeexplore.ieee.org, provided by the authors.

Color versions of one or more of the figures in this paper are available online at http://ieeexplore.ieee.org.

paired 3T and 7T images scanned from same subjects, and then propose a hierarchical reconstruction based on group sparsity in a novel multi-level Canonical Correlation Analysis (CCA) space, to improve the quality of 3T MR image to be 7T-like MRI. First, overlapping patches are extracted from the input 3T MR image. Then, by extracting the most similar patches from all the aligned 3T and 7T images in the training set, the paired 3T and 7T dictionaries are constructed for each patch. It is worth noting that, for the training, we use pairs of 3T and 7T MR images from each training subject. Then, we propose multi-level CCA to map the paired 3T and 7T patch sets to a common space to increase their correlations. In such space, each input 3T MRI patch is sparsely represented by the 3T dictionary and then the obtained sparse coefficients are used together with the corresponding 7T dictionary to reconstruct the 7T-like patch. Also, to have the structural consistency between adjacent patches, the group sparsity is employed. This reconstruction is performed with changing patch sizes in a hierarchical framework. Experiments have been done using 13 subjects with both 3T and 7T MR images. The results show that our method outperforms previous methods and is able to recover better structural details. Also, to place our proposed method in a medical application context, we evaluated the influence of post-processing methods such as brain tissue segmentation on the reconstructed 7T-like MR images. Results show that our 7T-like images lead to higher accuracy in segmentation of white matter (WM), gray matter (GM), cerebrospinal fluid (CSF), and skull, compared to segmentation of 3T MR images.

Index Terms

3T MRI; 7T MRI; canonical correlation analysis; image enhancement; magnetic resonance imaging (MRI); ultra-high-field MRI

I. Introduction

Magnetic Resonance Imaging (MRI) is widely used in medical imaging because of its non-invasive assessment of the body’s anatomy and physiology in both health and disease. In the clinical and research centers, usually high-resolution and high-contrast MRI is preferred because it provides significant structural details with a smaller voxel size. While, low-resolution MRI has fuzzy tissue boundaries with lower contrast. In the last decade, the ultra-high-field MR (7T) scanners were introduced, which allow high-resolution MRI scanning with many advantages in comparison to the routine MRI such as 3T MRI. Generally, the signal-to-noise ratio (SNR) of the MRI scanning has linear relation to the magnetic field [1]. For instance, 7T scanner provides about 2.3 times higher SNR than that of 3T scanner for the same spatial resolution. On the other hand, 7T MRI is able to provide images with higher resolution while maintaining similar SNR. Hereof, the recent researches show that 7T MRI is more helpful in the diagnosis and monitoring of diseases such as multiple sclerosis, cerebrovascular, brain tumors, and aging-related brain changes than 3T MRI [1], [2].

Another benefit of using 7T MRI, compared to 3T MRI, is that the tissue segmentation can be done much more accurately. For instance, the segmentation of MRI brain tissues in white matter (WM), gray matter (GM), and cerebrospinal fluid (CSF) using 7T MRI can be done with higher accuracy, compared to that of 3T MRI. Also, the segmentation of small brain structures such as hippocampal subfields is often difficult in 3T MR images, but more feasible in 7T MR images. In addition, in the case of low-quality and low-contrast cortical lesions and atrophies in the 3T MRI, the reconstructed 7T-like images will have higher quality and thus their tissue segmentations can be more accurate since 7T-like images are much closer to the ground-truth 7T images in terms of both tissue contrast and resolution. Therefore, 7T MRI has higher sensitivity to tissue changes and anatomical details, thanks to the higher tissue contrast and clearer tissue boundaries, as can be observed for the 3T and 7T MRI of the same subject in Fig. 1.

However, currently, 7T MRI scanners are more expensive and less available at hospitals and clinical centers, and thus most MR images are still acquired at routine 3T scanners. For example, in the world, the total number of 7T scanners is around 40, while there are over 20,000 3T scanners [3]. Therefore, it is of great interest to reconstruct 7T-like MR images from 3T MR images, to improve the quality of the input 3T MRI in terms of resolution and contrast. This motivates us to reconstruct 7T-like MR image from 3T MRI.

Reconstruction of high-resolution (HR) image from low-resolution (LR) image is the process of generating an image at a higher spatial resolution by using one or multiple LR images. In the past few decades, many methods have been proposed for HR image reconstruction in medical imaging and computer vision areas, which can be categorized into reconstruction-based methods [4]–[13], and example-based methods [14]–[38].

In the reconstruction-based methods, HR image reconstruction is considered as an inverse problem of recovering a HR image by assuming some degradation factors such as blurring and down-sampling, based on some prior knowledge about the observation model [4]. Since the details are missing in the LR image, one LR image may correspond to many HR images. As a result, the reconstruction problem is inherently ill-posed.

For this category of methods, there are some representative works in computer vision [4]–[7] and medical imaging areas [8]–[13]. For instance, in medical imaging, Islam [8] proposed a number of super-resolution methods to improve the resolution of 3D MRI volumes by using the prior models of the MRI data as regularization terms in an ill-conditioned inverse problem. In another work, Plenge [9] investigated reconstruction methods to increase the resolution in the slice selection direction and, as such, are an alternative to HR acquisition in terms of the SNR and acquisition time trade-offs. In [13], Woo *et al.* presented a super-resolution method for reconstruction of tongue by generating an image volume using three orthogonal images.

Example-based methods, also called learning-based methods, are more effective than the reconstruction-based methods because they are able to produce novel details that cannot be found in the LR image. They use paired LR and HR dictionaries, so that the high-frequency details, which are lost in a LR image, can be predicted from the corresponding HR dictionaries. In the example-based methods, first, the dictionaries of LR and HR image patch pairs for learning are constructed. Then, the LR image patches are represented, using the LR dictionary, to estimate the weights and then the estimated weights are used to estimate the desired HR image patches.

The representative works based on example-based methods can be divided into computer vision [14]–[29] and medical imaging areas [30]–[38]. For example, in computer vision, Gao *et al.* [18] presented a neighbor embedding-based algorithm for HR image reconstruction by combining the sparse neighbor search and subset selection based on Histogram of Gradient clustering. Yang *et al.* [19] proposed a support vector regression with sparse representation to generalize the modeling of relationship between images and their associated HR versions. Peleg *et al.* [20] proposed a statistical prediction model based on sparse representations of LR and HR image patches for single image super-resolution, which goes beyond the assumption of invariant sparse representation of low and high resolution dictionary pairs. Jiang *et al.* [21] proposed a coarse-to-fine face super-resolution approach via a multi-layer locality-constrained iterative neighbor embedding to represent the input LR patch while preserving the geometry of the original HR space. Yang *et al.* [25] proposed an example-based method for super-resolution of images by assuming that the LR and HR image patch pairs share the same sparse representation, with respect to LR and HR dictionaries.

In medical imaging, Rueda *et al.* [30] presented a sparse-based super-resolution method with paired HR and LR images, so that a HR version of a LR brain MR image can be generated. Zhang *et al.* [31] proposed a method for resolution enhancement of CT lung images based on a patch-based sparse representation. Bhavsar *et al.* [32] proposed a method for resolution enhancement of lung 4D-CT based on group sparse representation. Manjon *et al.* [33] proposed a super-resolution method for reconstruction of HR images from LR images using information from coplanar high resolution images of the same subject. In another work [34], Coupe *et al.* proposed a method to use a non-diffusion image to constrain the reconstruction of diffusion weighted images based on nonlocal patch-based strategy. Roy *et al.* [35] introduced an image restoration technique, called MR image example-based contrast synthesis (MIMECS), that recovers images with both the desired tissue contrast and a normalized intensity profile. Huynh *et al.* [36] proposed a method for estimation of CT image from MRI based on structured random forest and auto-context model. Alexander *et al.* [37] introduced a quality transfer method for diffusion MRI. Burgos *et al.* [38] proposed a method, named local image similarity (LIS), for the reconstruction of CT images from MR images.

In our work, we follow the example-based methods with sparse representation by incorporating the dictionary of 3T (LR) and 7T (HR) MR images. More specifically, our method is based on the idea that the information obtained in a high-resolution 7T MR image can be predicted from a low-resolution 3T MR image, with the additional prior information contained in the paired LR and HR dictionaries for the corresponding 3T and 7T patches. To generate the LR and HR dictionaries in the example-based methods, different techniques are incorporated, which include dictionary learning, local dictionary, and global dictionary. In the case of dictionary learning, the LR and HR dictionaries are jointly learned using a large number of LR and HR images to generate paired dictionaries for LR and HR images. In the case of local dictionary, for each patch of the input test LR image, the LR patches and their corresponding HR patches are extracted from its neighborhood region in the training sets of LR and HR images to generate the LR and HR dictionaries, respectively. In the case of global dictionary, all the patches from different locations of LR and HR training images are extracted. Then, for each patch of the input LR image, a fraction of the LR patches and their corresponding HR patches are extracted based on the similarity to the input LR image. In our paper, to generate the 3T and 7T dictionaries, we use both the local dictionary and global dictionary, which will be explained in more detail below.

Also, the example-based methods assume that the images of LR and HR spaces are highly correlated and have similar distributions, yet this assumption may not be completely satisfied. To overcome this weakness, Huang *et al.* [41] use canonical correlation analysis (CCA) to map the LR and HR images into a common space, in which the LR and HR images have higher correlation. However, mapping the LR and HR images into the CCA space only increases the correlation between all pairs of patches in the 3T and 7T dictionaries, while it is of great interest to further increase the correlation of the most important patches of the 3T and 7T dictionaries in representation of the input 3T patch to reconstruct 7T-like patch. This means that, by mapping the whole 3T and 7T dictionaries into CCA space, the optimization function of CCA may be affected by many patches that are not used in the representation of the input 3T patch, so by selecting a subset of 3T and 7T dictionaries, the correlation can be further increased.

Accordingly, we propose an extension of CCA, called multilevel CCA, to further increase the correlation of 3T and 7T dictionaries by considering the representation of the input 3T patch with respect to the 3T dictionary. In addition, we employ the group sparsity in the multi-level CCA space to achieve structural consistency among the nearby 3T patches for more accurate reconstruction. Also, we introduce a hierarchical framework for the reconstruction of the rough structure of the 7T MR image at the initial step and the fine details at the final step. To the best of our knowledge, our proposed method is the first one for the reconstruction of 7T MR images from 3T MR images. A preliminary version of this work was presented at a conference [42]. The work is significantly extended in this article by: 1) adding more methodological details, experimental results, validations, and discussions; 2) increasing the number of subjects; 3) adding global dictionary to the proposed method; 4) comparing with other methods in the context of medical imaging; 5) adding more metrics for quantitative comparison, such as VIF, UQI, and SSIM; 6) evaluating performance on tissue segmentation; and 7) evaluating 7T-like reconstruction in the presence of atrophy.

This paper is presented as follows. In Section II, we propose our 7T-like image reconstruction method. Experimental results are given in Sections III–V. Section VI provides the conclusion and discussion of the paper.

II. Proposed Method

A. Overview

We propose a hierarchical reconstruction based on group sparsity in a novel multi-level CCA, to improve the quality of 3T MR image to be 7T-like MRI, as shown in Fig. 2. First, all the overlapping patches are extracted from the input 3T MR image. Then, for each input 3T MRI patch, the most similar patches from all the aligned 3T and 7T training images are used to build the paired 3T and 7T dictionaries. Then, our proposed multi-level CCA is incorporated to map the paired 3T and 7T patch sets into a common space to increase their correlation. In such space, each input 3T patch is sparsely represented by the 3T dictionary and then the obtained sparse coefficients together with the corresponding 7T dictionary are used to reconstruct the 7T-like patch. Also, to have the structural consistency between adjacent patches, the group sparsity is employed. This reconstruction is performed by reducing patch size in a hierarchical framework. In the following sections, the details of our method is provided.

B. Dictionary Building

In this section, we build 3T and 7T dictionaries for each input 3T MRI patch. We use two strategies to generate dictionaries, namely local dictionary and global dictionary. The local dictionaries are the representatives of local anatomical structure and can be used for the reconstruction of the to-be-estimated 7T-like patches, due to two reasons. First, in reconstruction of 7T-like MRI from 3T MRI, the images are aligned and have similar structures, which allow us to benefit such similarity by constructing the local 3T and 7T dictionaries. Second, since the neighboring patches in an image are highly correlated, the patches in the local 3T and 7T dictionaries should have similar structure to the input 3T MRI, as well as the to-be-estimated 7T MRI. To create a local dictionary for an input 3T patch, the input 3T image needs to be aligned with the training 3T image set. To do that, the input 3T image is affine aligned to the training 3T images using a two-step strategy. First, all training images are affine aligned to a MNI template [46]. Then, the input 3T image is affine aligned to the MNI template. In such case, all the training 3T images and thus their patches in the local dictionary have similar anatomical structure to the input 3T patch. Let $\mathbf{y}$ be a 3T patch with size of $m \times m \times m$ which is extracted from the input 3T MR image $\mathbf{Y}$. For $\mathbf{y}$, the local 3T dictionary $\mathbf{D}_{3T}$ and 7T dictionary $\mathbf{D}_{7T}$ are built by extracting the patches from the same location and nearby locations in a search window size of P in all N pairs of aligned 3T and 7T training MR images from N training subjects.

In contrast to local dictionary, the global dictionary is constructed from all the patches across the whole image. Generally, the local dictionary may not be able to reconstruct lesion and atrophy, if they do not appear in the neighboring region of the voxel location in the input 3T image. In contrast, global dictionary could provide such information if similar patches could be found in other regions in the brain. To generate the global LR and HR dictionaries, we extract all the patches from LR and HR training images. In such case, for each patch of the input LR image, a fraction of the LR patches and their corresponding HR patches are extracted based on the similarity to the input LR image. To do so, we can build the global 3T dictionary and $\mathbf{D}_{3T}$ 7T dictionary $\mathbf{D}_{7T}$ for $\mathbf{y}$ by extracting all the patches from pairs of aligned 3T and 7T training MR images. Then, for each input 3T patch we select top 100 most similar ones from the 3T patches and their corresponding 7T patches, which will be used for the representation of the input 3T patch.

C. Multi-Level CCA Representation

Following the building of 3T and 7T dictionaries (local or global), in this section we aim to reconstruct the 7T-like patch $\mathbf{x}$ from the 3T input patch $\mathbf{y}$ using $\mathbf{D}_{3T}$ and $\mathbf{D}_{7T}$. First, $\mathbf{y}$ is sparsely represented with respect to the dictionary $\mathbf{D}_{3T}$ via

$$\hat{\boldsymbol{\alpha}} = \arg\min \|\mathbf{y} - \mathbf{D}_{3T}\boldsymbol{\alpha}\|_2^2 + \lambda_1 \|\boldsymbol{\alpha}\|_1 \quad (1)$$

where $\boldsymbol{\alpha}$ denotes the estimated sparse coefficients in the column vector representation. Then, $\boldsymbol{\alpha}$ can be used together with $\mathbf{D}_{7T}$ to reconstruct $\mathbf{x}$, as follows

$$\mathbf{x} = \mathbf{D}_{7T}\hat{\boldsymbol{\alpha}}. \quad (2)$$

The sparse representation in the spatial domain assumes that the 3T (LR) and 7T (HR) images are highly correlated and have similar distributions, however, such assumption may not be held completely in practice. To overcome this weakness, the sparse representation can be done in the CCA space. In general, CCA is utilized to increase the correlation between the projections of two sets of variables in the CCA space by mapping them based on two basis vectors [41]. Here, to increase the correlation of the two dictionaries $\mathbf{D}_{3T}$ and $\mathbf{D}_{7T}$, we use CCA by calculating the basis vectors $\mathbf{b}_{3T}$ and $\mathbf{b}_{7T}$. In such case, $\mathbf{D}_{3T}$ and $\mathbf{D}_{7T}$ in CCA space (i.e., $\mathbf{b}_{3T}\mathbf{D}_{3T}$ and $\mathbf{b}_{7T}\mathbf{D}_{7T}$) have higher correlation compared to image space. To perform the sparse representation in the CCA space, the 3T MRI patch $\mathbf{y}$ is similarly projected into CCA space using the basis vector $\mathbf{b}_{3T}$. Then, $\mathbf{y}$ is sparsely represented with respect to $\mathbf{D}_{3T}$ in CCA space by adjusting (1) as

$$\hat{\boldsymbol{\alpha}} = \arg\min \|\mathbf{b}_{3T}\mathbf{y} - \mathbf{b}_{3T}\mathbf{D}_{3T}\boldsymbol{\alpha}\|_2^2 + \lambda_1 \|\boldsymbol{\alpha}\|_1. \quad (3)$$

Although the correlation between all patch pairs in the $\mathbf{D}_{3T}$ and $\mathbf{D}_{7T}$ dictionaries can be increased using CCA, by using the whole 3T and 7T dictionaries, the computation of transformation matrices of CCA may be affected by many patches that are not used in the final representation of the input 3T patch. To address this problem, the mapping to the CCA space can be done only on a subset of the 3T and 7T dictionaries which is more representative in sparse representation of the input 3T patch $\mathbf{y}$, to further increase the correlation.

This intuition motivates us to propose multi-level CCA (an extension of CCA), to effectively improve the correlation of $\mathbf{D}_{3T}$ and $\mathbf{D}_{7T}$ based on the input 3T patch. To illustrate the concept of multi-level CCA, we use the red circles and green circles corresponding to the patches of dictionaries $\mathbf{D}_{3T}$ and $\mathbf{D}_{7T}$ in Fig. 3. In image space, the correlation between the paired 3T and 7T image patches of $\mathbf{D}_{3T}$ and $\mathbf{D}_{7T}$ may not be high as shown in Fig. 3. After CCA projection, the correlation between the paired 3T and 7T image patches is increased. However, increasing the correlation without considering the content of the input 3T patch does not address the problem of assuming the same sparse representation of 3T and 7T image patches. By considering a subset of 3T and 7T dictionaries which is more representative in sparse representation of the input 3T patch, the correlation can be further improved.

So, in the first level CCA, we use (3) in CCA space to sparsely represent the input 3T patch **y** using 3T dictionary $\mathbf{D}_{3T}$. In such case, the non-zero sparse coefficients indicate the most important patches of $\mathbf{D}_{3T}$ in representation of the input 3T patch. In the 2nd level CCA, rather than the whole dictionaries $\mathbf{D}_{3T}$ and $\mathbf{D}_{7T}$, a subset of $\mathbf{D}_{3T}$ which is more representative of input 3T patch (non-zero sparse coefficients), is mapped from the image space into the CCA space together with the corresponding subset of $\mathbf{D}_{7T}$ (Fig. 3(b)). Then, in the 2nd level, we sparsely represent the input 3T patch using this subset of 3T dictionary. Using such dictionary refinement, in the next level, the reconstruction using the learned sparse coefficients is more effective. Such process can be performed in L levels to further refine the dictionaries for improving the representation of the input 3T patch. At each level, input 3T patch is sparsely represented with respect to 3T dictionary using (3). Then, the most representative patches of 3T and 7T dictionaries corresponding to the non-zero coefficients, will be mapped from image space to the CCA space, in the next level. It should be mentioned that, at each level of multi-level CCA, the new set of basis vectors $\mathbf{b}_{3T}$ and $\mathbf{b}_{7T}$ are calculated from the refined $\mathbf{D}_{3T}$ and $\mathbf{D}_{7T}$ dictionaries.

After L-th level CCA projection, the input 3T patch is sparsely represented using the subset of 3T dictionary. Then, the sparse coefficients are incorporated together with the subset of 7T dictionary in reconstruction of 7T-like patch.

D. Group Sparse Regularization

In patch-based reconstruction, using (3) individually for sparse representation of each local patch, does not guarantee the compatibility between adjacent patches. Besides, neighboring patches often have similar structures and should have similar sparse representation. By considering a patch and its adjunct patches as a group, we can enforce group sparsity to nearby patches for local structure consistency.

Therefore, after mapping of the images from image space to multi-level CCA space, rather than sparse representation of a single 3T patch, we enforce group sparsity among the input 3T patch and the immediate neighboring 3T patches. In such case, the group sparsity shares the same sparse representation to make consistency in the local structure. By referring to the input patch and its G immediate neighbors as a group, in addition to the sparse representation of the input 3T patch, the sparse representation can be solved simultaneously, for G neighboring patches, to estimate the coefficients for the whole group. To incorporate the group sparsity in the multi-level CCA, we reformulate (3) as

$$\hat{\mathbf{A}}=\arg\min\sum_{i=1}^{G+1}\|\mathbf{b}_{3T,i}\mathbf{y}_i-\mathbf{b}_{3T,i}\mathbf{D}_{3T,i}\boldsymbol{\alpha}_i\|_2^2+\lambda_1\|\mathbf{A}\|_{2,1} \qquad (4)$$

where the first term is multi-task least square error for the input patch and it's G neighboring patches (totally G+1 patches). $\mathbf{D}_{3T,i}$ is the 3T dictionary, $\mathbf{y}_i$ is the input 3T patch, and $\boldsymbol{\alpha}_i$ denotes the sparse coefficient vector of the i-th patch in the group. $\mathbf{A} = [\boldsymbol{\alpha}_1,\ldots,\boldsymbol{\alpha}_{G+1}]$ includes the sparse coefficients vectors of G+1 patches in the group. The second term is used for the regularization, in which the L_2 norm is applied to each row of **A** to ensure the neighboring patches have similar sparsity, while the L_1 norm is applied to all the columns of $\mathbf{A}$ to ensure the sparsity.

E. Hierarchical Reconstruction

Based on the proposed group sparsity in multi-level CCA space, each patch of input 3T MR image can be used to reconstruct the corresponding 7T-like MRI patch. However, in the patch-based reconstruction, choosing a suitable size for the patches is of great importance. For instance, by choosing a small size for the patches, the details can be captured, but the predicted 7T-like image would be noisy and unreliable. In contrast, if a large size is chosen for the patches, the whole structure can be captured, but the predicted 7T-like image would be fuzzy. In [45], Hertzman *et al.* used the iterations by changing patch size to update synthesized image. In our work, to overcome this problem, we propose a changing patch size scheme for the reconstruction. By starting from a large patch size, the size of patches is hierarchically reduced in multi-iterations. In the first iteration, an initial 7T-like image is reconstructed to achieve the whole structure. Then, in the subsequent iterations, 7T-like image is hierarchically reconstructed by gradually reducing the patch size to recover the image details, as explained below.

- First iteration: Reconstruction of initial 7T-like image. Using (4), each input 3T patch $\mathbf{y}$ is sparsely represented using the dictionary $\mathbf{D}_{3T}$. Then, the sparse coefficients are used together with the $\mathbf{D}_{7T}$ to estimate the corresponding 7T-like patch $\mathbf{x}$. By averaging the overlapped 7T-like patches, the whole 7T-like image is reconstructed.
- The subsequent iterations: Hierarchical reconstruction of 7T-like image. By incorporating the initial 7T-like image, we propose (5) to reconstruct the 7T-like image in the subsequent iterations (2nd to K-th), by adding a regularization term to (4) as

$$\hat{\mathbf{A}}^k = \arg\min \sum_{i=1}^{G+1} \|\mathbf{b}^k_{3T,i}\mathbf{y}^k_i - \mathbf{b}^k_{3T,i}\mathbf{D}^k_{3T,i}\boldsymbol{\alpha}^k_i\|_2^2 + \lambda_1\|\mathbf{A}^k\|_{2,1} + \lambda_2\sum_{i=1}^{G+1}\|\mathbf{b}^k_{7T,i}\mathbf{x}^{k-1}_i - \mathbf{b}^k_{7T,i}\mathbf{D}^k_{7T,i}\boldsymbol{\alpha}^k_i\|_2^2. \qquad (5)$$

In (5), $k = \{2,\ldots,K\}$ is the iteration number and $\mathbf{x}_i^{k-1}$ represents a reconstructed 7T-like patch in the iteration $k-1$. The first and second terms are same as those in (4), and the last term is the penalty term, which is proposed to use the reconstructed 7T-like image in the previous iteration as a guidance to reconstruct the 7T-like image in the current iteration. Actually, the last term has been proposed to ensure consistency between iterations.

After reconstruction of the 7T-like patches, we incorporate the inverse of basis vector $\mathbf{b}_{7T}$ to map the 7T-like patches from the CCA space to the image space. The pseudo-code of our proposed method is given in Algorithm 1.

Algorithm 1

7T-like MRI reconstruction from 3T MRI

```
Input: A test 3T MRI and $N$ pairs of training aligned 3T and 7T MRI.
Output: Reconstructed 7T-like MRI for the test 3T MRI.
For each local patch:
   1. Partition the input 3T MRI into overlapped patches $\mathbf{y}$ of size $m \times m \times m$ with one voxel shift.
   2. Generate 3T and 7T dictionaries $\mathbf{D}_{3T}$ and $\mathbf{D}_{7T}$ for each patch by extracting the patches from $N$ training pairs of aligned 3T and 7T MRI.
   3. Transform $\mathbf{D}_{3T}$ and $\mathbf{D}_{7T}$ into CCA space using $\mathbf{b}_{3T}$ and $\mathbf{b}_{7T}$.
   4. Use (4) to estimate the sparse coefficients $\mathbf{A}$ by considering each patch and its $G$ neighborhood as a group.
   5. Transform a subset of $\mathbf{D}_{3T}$ and $\mathbf{D}_{7T}$, corresponding to non-zero sparse coefficients, into CCA space using $\mathbf{b}_{3T}$ and $\mathbf{b}_{7T}$.
   6. Repeat the steps 4 and 5 for $L$ times, where $L$ is the number used in multi-level CCA.
   7. Reduce the patch size.
   8. Use (5) to estimate the sparse coefficients $\mathbf{A}$.
   9. Reconstruct the 7T-like patch by multiplying the 7T dictionary $\mathbf{D}_{7T}$ with the estimated sparse coefficients.
  10. Repeat the steps 1 to 9 $K$ for iterations.
  11. Reconstruct the final 7T-like image by taking the average of all reconstructed 7T-like patches if they are overlapped.
End
```

III. Experimental Results

We evaluated the performance of our proposed method by comparing with related works, including histogram-based method, sparse representation in image space [25], sparse representation in CCA space [41], MIMECS [35], LIS [38], and RF [36], as briefly introduced below.

Histogram-based method is considered to be a baseline method and implemented as follows. Given a set of training 3T and 7T images. First, the histograms of all the training 3T and 7T images are used to generate the dictionaries of the 3T and 7T images, by defining each atom of the dictionary as the vector of histogram bins. For a given input 3T image, its histogram, which is represented by a vector of histogram bins, can be sparsely represented by the dictionary of 3T images and then the sparse coefficients are used to generate the histogram of to-be-estimated 7T-like image. Then, the 7T-like image is reconstructed by matching the input 3T image to the estimated histogram.

As mentioned in the introduction section, sparse representation method in image space [25] has been proposed for super-resolution of natural images and face images. In [25], using a large set of training images, LR and HR dictionaries are jointly learned to reconstruct a HR image from a LR image. In our paper, we use both dictionary learning and local dictionary strategies to compare with this method. In the first strategy, we train the 3T and 7T dictionaries jointly, using the whole 3T and 7T images, to generate paired dictionaries for 3T and 7T images. In the second strategy, similar to our proposed method, we consider local dictionaries.

Sparse representation method in CCA space [41] has originally been proposed for super-resolution of face images. To use this method for comparison, we consider building local dictionaries similarly as our method.

We also used other three state-of-the-art algorithms for the reconstruction of 7T from 3T MRI, as the comparison methods. These methods include MIMECS [35], previously proposed for the restoration of MR images with both desired tissue contrast and normalized intensity profile; LIS [38], proposed for the reconstruction of CT images from MR images; and random forest, proposed for reconstruction of CT from MR images. We re-implemented the MIMECS for reconstruction of 7T from 3T MRI with the following settings and parameters. We considered patches of dimension $3 \times 3 \times 3$ voxels. For the dictionary construction, since the size of MR images is $180 \times 260 \times 300$, so the global dictionary could be very large. So, we construct a dictionary for each patch with size of 100, by selecting the most similar 100 3T MRI patches to the input 3T patch from the global collection of all the patches. For the sparsity regularization term, we selected λ=0.2 to achieve the best visual and numerical results.

We re-implemented the LIS for reconstruction of 7T MRI from 3T MRI with the following settings and parameters. We register the corresponding 3T and 7T images using FLIRT in FSL package with a 9-DOF transformation, to minimize the possible global distortions. We examined two similarity measures, including convolution-based fast local normalized correlation coefficient (LNCC) and local normalized sum of square differences (NSSD). We implemented the LNCC using the local correlation coefficient (1) in [38] which was been extended in [39], by calculating the local mean, local standard deviation, and local correlation at each voxel using convolution based on Gaussian kernel. Followed by the calculation of the local correlation coefficient for all voxels, the intensity similarity measure is calculated by summing the local correlation coefficient for all voxels. To implement the NSSD, we used the (2) in [38], which is based on the mean and standard deviation of the patches followed by convolving with a Gaussian kernel. We examined LNCC and NSSD using Gaussian kernels with different standard deviations. By trying different parameters, we found LNCC with standard deviation equal to 5 results the best. Also, we converted the ranked LNCC and NSSD to weights by applying an exponential decay function ((3) in [38]) with beta parameter. We examined the beta in the range of [0.1 0.2 … 1] and we found beta = 0.5 had the best result.

A. Data and Preprocessing

We recruit 13 volunteers, with ages of 30 ± 8 years, for our study. Of these 13 volunteers, 8 subjects were healthy and 5 subjects were patient with epilepsy. They were scanned using both 3T and 7T scanners. T1 images of 224 coronal slices were obtained in a 3T Siemens Trio scanner with a 3D MP-RAGE sequence using image parameters: TR = 1900 ms, TE = 2.16 ms, TI = 900 ms. Flip Angle = 9°, and resolution = $1 \times 1 \times 1\text{mm}^3$. T1 images of 191 sagittal slices were obtained in a Siemens Magnetom 7T whole-body MR scanner with a 3D MP2-RAGE sequence using image parameters: TR = 6000 ms, TE = 2.95 ms. TI = 800/2700 ms. FlipAngle = 4°/4°, and resolution = $0.65 \times 0.65 \times 0.65\ \text{mm}^3$. Based on our observations, we found minimal distortions between the obtained 3T and 7T images as these images were acquired with a gradient echo sequence. As for alignment, we register the corresponding 3T and 7T images using FLIRT in FSL package with a 9-DOF transformation, to minimize the possible global distortions. A skull stripping step is followed to remove the non-brain tissues [47].

Also, since MRI image intensities usually vary from scan to scan and subject to subject, we normalize all the MR images to have similar intensity range. First, the input 3T, and all the training 3T and 7T MR images are normalized into [0, 1] using $y = y - min(y)/max(y) - min(y)$, where y is the voxel value, $max(y)$ and $min(y)$ are the maximum and minimum values within the MR image. Then, we use histogram matching from all the training 3T images to the input 3T image to ensure that all the 3T images have similar intensity and contrast ranges. Similarly, we apply histogram matching on 7T images by selecting one as reference to be matched with all other 7T training images for ensuring that all the training 7T images have similar contrast ranges.

B. Experiment Settings

For evaluation, we adopt leave-one-out cross-validation by considering one 3T MR image for testing and the rest 12 pairs of aligned 3T and 7T MR images for training. We consider $L = 4$ levels for multi-level CCA. Also, we consider $G = 6$ neighboring patches for each input 3T patch in the group sparsity. We set $\lambda_2 = 0.1$, while we consider different values for λ_1 based on different CCA levels and iterations, as will be discussed in the Section III-G. In the hierarchical framework, we consider $K = 3$ iterations where the size of patches ($m \times m \times m$) is reduced from 7 × 7 × 7, 5 × 5 × 5 to 3 × 3 × 3. Also, to generate the local dictionary, from the first to the third iteration, the neighborhood size P is set to 13 × 13 × 13, 11 × 11 × 11 and 9 × 9 × 9, respectively. In addition, we select the overlap of 1 voxel between the adjacent patches, and the overlapping regions to be averaged when reconstructing the 7T-like image. Our proposed method was implemented in MATLAB R2014b environment, running on an iMAC with Intel Quad core i7 (3 GHz) and 16 GB of RAM. It takes around 4hr to reconstruct a full 7T MR image of size 180 × 260 × 300.

For the previous methods, the experimental settings are also chosen appropriately for their best performances. For instance, the histogram-based method is applied to the whole image, and we consider the patch size of 3 × 3 × 3 (for sparse representation [25] and CCA [41]), which is in the same size as the third iteration of our method.

C. Visual Inspection

In this section, we use an experiment to evaluate our proposed method by comparing it to previous methods. We compare the reconstructed 7T-like MRI based on the histogram-based method, sparse (dict. learning) [25], sparse (local dict.) [25], CCA [41], MIMECS [35], LIS [38], RF [36], our proposed method (global dict.), and our proposed method (local dict.), as shown in Figs. 4 and 5. The first, third, and fifth rows show the axial, sagittal and coronal views of the reconstructed 7T-like image of a subject using different methods, respectively. The second, fourth and sixth rows show the close-up views of part of the reconstructed 7T-like image for the axial, sagittal and coronal views, respectively. Compared to all of the previous methods, the reconstructed 7T-like image using our proposed method is closer to the ground-truth 7T on the right column of Fig. 4. Also, it contains much more details than previous methods, while the results of previous methods are blocky or blurry.

In histogram-based method, the close-up views clearly show poor quality of reconstructed 7T-like image compared to the ground-truth 7T. Compared to our method, the reconstructed 7T-like image by histogram-based method is blocky, especially in the boundary between white matter and gray matter.

Sparse (dict. learning) [25] and sparse (local dict.) [25] have fuzzy results. The reason is that, the correlation of 3T and 7T images is not high enough to use the same sparse representation in LR and HR spaces. CCA [41] has better results than sparse representation because of sparse representation in CCA space, in which the 3T and 7T images have higher correlations. MIMECS [35] and LIS [38] have similar limitations as sparse method, since both assume the same representation can be used in LR and HR spaces. RF [36] has better result than sparse representation based methods, because it does not assume the LR and HR spaces have high correlation. However, compared to our proposed method, it had worse results, caused by the lack of multi-level CCA, group sparsity, and hierarchical structure as used in our proposed method.

D. Evaluation of Intermediate Results

In this experiment, we evaluate our method by comparing the output of different steps of our proposed method with the previous methods. Fig. 6 shows the error maps of the axial view by averaging all subjects based on the output of different steps of our proposed method, including multi-level CCA, group sparsity, and hierarchical structure by comparing with sparse (local dict.) [25] and CCA [41] methods. The error maps of the other two views (sagittal and coronal views) could be found in Fig. 1 in the supplementary material are available in the supplementary files/multimedia tab. Also, the axial, sagittal and coronal views of a subject together with the error maps based on the output of different steps of our proposed method, by comparing with the previous methods, have been shown in Fig. 2 in the supplementary material are available in the supplementary files/multimedia tab. For each of the axial, sagittal and coronal views, the ground-truth is shown on the right column of the figure. The error maps are generated based on the difference between the ground-truth 7T and the reconstructed 7T-like images by each method. The color map ranges from red to blue, where the red color indicates the highest error and the blue color reveals the least error. Based on the axial, sagittal and coronal views, the result of multi-level CCA is generally better than sparse (local dict.) [25] and CCA [41], due to the incorporation of the content of input 3T patches to improve the correlation of 3T and 7T local dictionaries. The output of our proposed method, after multi-level CCA and group sparsity, is further improved because of the enforcement of sparsity among neighboring patches, which leads to more reliable sparse representation. By using the hierarchical structure, the final result is more reliable. These result further confirm the superiority of our proposed method, when compared to the previous methods.

E. Quantitative Comparison

In this section, we examine our reconstructed 7T-like image numerically by comparing with the previous methods and the ground-truth 7T MR image of the same subject. We use four measures, i.e., peak-signal-to-noise ratio (PSNR), visual information fidelity (VIF), universal quality index (UQI), and structural similarity (SSIM). PSNR is defined as the ratio between the maximum intensity value of the ground-truth image and the power of corrupting noise (i.e., the average sum of square differences between the ground-truth image and reconstructed image). VIF is defined as an information fidelity criterion that quantifies the Shannon information of the image. UQI is defined by modeling the image distortion as a combination of loss of correlation, luminance distortion, and contrast distortion. SSIM measures the quality of an image using mean, variance and cross-correlation. Higher PSNR, VIF, UQI, and SSIM reveal that the reconstructed images are much closer to the ground-truth 7T image. Table I compares the average and standard deviation of measurements for all 13 subjects by histogram-based method, sparse [25] (local dict.), sparse [25] (dict. learning), CCA [41], MIMECS [35], LIS [38], RF [36], our method with local dictionary, and our method with global dictionary. The detailed comparison of PSNR, VIF, UQI and SSIM on these 13 subjects could be found in Table I in the supplementary material are available in the supplementary files/multimedia tab. Compared to the previous methods, our proposed method has a much higher PSNR, VIF, UQI, and SSIM for all 13 subjects. Also, we performed permutation test in Table II to show that the improvement of our result compared to the previous methods is significant. The result showed that the improvement is statistically significant ($p < 0.01$ by permutation test).

F. Comparison With Patch Similarity-Based CCA Method

In this experiment, we evaluate the performance of our proposed method with a variation of CCA method, called patch similarity-based CCA method, in Table III. In this method, for each patch of the input 3T image, a certain percent of the most similar 3T patches to the input 3T image patch and their corresponding 7T patches are extracted from a neighborhood search window to generate the local 3T and 7T dictionaries. Then, followed by the CCA transformation, the input 3T patch is sparsely represented with the subset of 3T dictionary and then the estimated coefficients are used together with the subset of 7T dictionary to reconstruct the 7T-like patch. We compare the result of our proposed method with this patch similarity-based CCA method when 100%, 80%, 60%, 40%, 20%, and 10% of the most similar patches in the neighborhood search window are used to build the local 3T and 7T dictionaries, respectively. The results reveal that, by selecting the most similar patches in the neighborhood search window, the performance will be improved, but still worse than our proposed method.

G. Effects of Parameters

In this section, we discuss the effects of some important parameters on the performance of our proposed method.

In the hierarchical architecture, we chose three iterations ($K = 3$) where the patch size is changed from 7 × 7 × 7, 5 × 5 × 5 to 3 × 3 × 3 from the first to the third iteration, respectively. Although a higher number of iterations can be considered at the cost of additional computational complexity, we found that hierarchical reconstruction, with three iterations, performs well with a coarse-to-fine reconstruction. By considering the patch size of 7 × 7 × 7 in the first iteration, we can capture the entire structure of local regions. In the last iteration, we consider 3 × 3 × 3 patches to achieve the finest resolution. Although a larger patch size can be considered as the first iteration, it does not help to significantly improve the result of our method, while also increasing the computational complexity.

Accordingly, for the first, second and third iterations, the neighborhood size for local dictionary building is set to 13 × 13 × 13, 11 × 11 × 11 and 9 × 9 × 9, respectively. Fig. 7 shows the mean performance of all subjects for the first, second and third iterations by considering different search window size for the reconstruction of 7T-like images. From the curves, it can be observed that, generally, by increasing the search window size, the performance is improved. The reason is that, by using a larger search window size, the size of local dictionaries is increased.

Intuitively, larger local dictionaries should have more expressive power in the representation of 3T patches, thus yielding more accurate 7T-like reconstruction in the cost of higher computational complexity. The appropriate search window size is chosen as a tradeoff between the quality of reconstructed 7T-like image and the computational time. We find that choosing the search window size of 13 × 13 × 13, 11 × 11 × 11, and 9 × 9 × 9 for the first, second, and third iterations yields to a good quality for the reconstructed 7T-like image. Also, we perform a t-test to evaluate the PSNR changes for different window sizes. Based on the two-sample t-test, by increasing the search window size from 9, 7, 5 to 13, 11, 9 for the first, second and third iterations, respectively, the p-values are 0.0023, 0.0011, and 0.0003. Therefore, the improvement of PSNR is significant (all $p < 0.01$). However, by further increasing the search window size to 17, 15 and 13 for the first, second and third iterations, respectively, the improvement is not quite statistically significant, because the p-values are 0.5651, 0.8465, and 0.6305, respectively. Thus, in our experiments we just selected the search window sizes of 13, 11 and 9 for the first, second and third iterations, respectively.

To see the impact of the number of CCA levels L in multilevel CCA, in Fig. 8 we show the mean performance of our proposed method, in terms of PSNR, based on different L values for reconstruction of 7T-like images of all subjects. Generally, by increasing the number of levels L, the PSNR is increased. The reason is because, at each level, a subset of 3T dictionary (which has more power in representation of input 3T patch) is selected as the next level representation. However, after four levels ($L = 4$), the improvement is negligible. We have performed two-sample t-test to see the improvement of PSNR in multi-level CCA for each iteration. For the first, second and third iterations, the p-values are 0.0030, 0.0020, 0.0023, respectively. Therefore, we can conclude that all these p-values are smaller than 0.01, $p < 0.01$, and thus the improvement is considered to be statistically significant.

Therefore, in the current experimental setting, we consider four levels. However, since the proposed multi-level CCA is a general framework, more than four levels can still be considered to further increase the correlation of 3T and 7T local dictionaries with respect to the input 3T MRI in the cost of higher computational complexity.

Since the core of our proposed method is based on sparse representation, the sparsity parameter λ_1 should be chosen appropriately to help achieve the best qualitative and quantitative results for the reconstruction of 7T-like images. It is worth noting that choosing the sparsity parameter λ_1 relates to both the patch size and the size of local 3T dictionary. Since the patch size is different at each iteration of the hierarchical reconstruction and also the size of local 3T dictionary is different at each level of the multi-level CCA, the sparsity parameter λ_1 should be appropriately chosen for each iteration and each level. Fig. 9 shows the best chosen λ_1 at each iteration of hierarchical reconstruction by increasing the number of CCA levels from 1 to 4. Generally, from the first to the last iteration, λ_1 should be chosen smaller, while by increasing the number of CCA levels, λ_1 should be chosen larger, in order to achieve better results for reconstruction of 7T-like images. Table IV shows the number of selected dictionary elements with respect to different values of the chosen λ_1 at each level of multi-level CCA (with totally three iterations). Based on the search window sizes of $13 \times 13 \times 13$, $11 \times 11 \times 11$, and $9 \times 9 \times 9$ for the first, second, and third iterations, the original local 3T dictionaries have 26364, 15972, and 8784 patches, respectively. At each iteration, by increasing the number of levels in the multi-level CCA, a smaller subset of local dictionary is selected for the next level. For instance, at the level 1, 6850 out of 26364 patches (which correspond to 26% of the original local dictionary size) have non-zero coefficients in λ_1. At level 2, 1580 out of 6850 patches (which correspond to 23% of the dictionary size in level 1) have non-zero coefficients in λ_1, and so on.

From the first to the last iteration, the patch size should become smaller and smaller. This is because for larger patch size, there is less chance for the patches in the local dictionary to be similar to the input test 3T patch; thus a larger sparsity parameter is needed to enforce sparsity for the representation of the input test 3T patch. On the other hand, for the smaller patch size, a larger number of patches will be similar to the input test 3T patch. Thus, by choosing smaller sparsity parameter λ_1, less sparsity is applied and more patches can have a chance to represent the test 3T patch. By increasing the number of CCA levels, the size of local dictionary becomes smaller; thus, choosing a larger sparsity parameter λ_1 allows achieving more accurate results. To select the best λ_1, we used the cross-validation on the training set.

IV. Evaluation for Tissue Segmentation

We evaluate the influence of the reconstructed 7T-like image on brain tissue segmentation, where the brain tissues are separated into WM, GM, CSF and skull. We compare the segmentation results of the original 3T MRI and the reconstructed 7T-like images by the histogram-based method, sparse representation [25], CCA [41], MIMECS [35], LIS [38], RF [36], our method with local dictionary, and our method with global dictionary. Here, we consider the segmentation result of 7T MRI as the ground-truth. We utilized the SPM12 [40] for brain tissue segmentation.

Fig. 10 shows the segmentation results for the axial view of one subject, together with the close-up view of three selected regions, based on the original 3T MRI, the reconstructed 7T-like images by different methods, and 7T MRI. These visual results indicate that, compared to all the previous methods, the segmentation result by our proposed method is closer to the segmentation of the ground-truth 7T image.

Also, as for quantitative comparison, the average Dice Ratio of segmentation maps of WM, GM CSF and skull for all 13 subjects is shown in Fig. 11. Generally, the segmentation result by our method significantly outperforms the results from direct segmentation of 3T MRI and also the results from reconstructed images of all previous methods, for all WM, GM, CSF and skull segmentations ($p < 0.01$).

V. Evaluation for Reconstruction of 7T-Like Images With Brain Atrophy

In this experiment, we evaluate our proposed method for reconstruction of 7T-like images of patient with atrophy. Fig. 12 shows 3T image, 7T image and the reconstructed 7T-like brain region of a patient with two atrophies close to the right and left hippocampus areas, shown by red arrows. In 3T MRI, the regions can be observed with lower contrast and resolution, compared to 7T MRI. By reconstruction of 7T-like image, the areas can be seen with higher resolution and contrast.

VI. Conclusion and Discussion

We proposed a hierarchical framework based on a novel multi-level CCA and group sparsity, to improve the quality of 3T MR image to be 7T-like MRI. We were provided with an input 3T MR image and a set of pairs of aligned 3T and 7T images in the training set. It should be mentioned that, 7T images were used (paired with 3T counterpart) only for training and learning the parameters of the group sparsity and multi-level CCA. For any given 3T, once training and parameter learning has been done, 7T-like images will be generated. In this paper, the objective was the reconstruction of 7T-like image from the input 3T MR image based on the training set which includes the 3T and 7T MR images scanned from each training subject. First, the input image was partitioned into overlapping patches. Then, for each patch, the local 3T and 7T dictionaries were constructed from all aligned subject images in the training set. We proposed multi-level CCA space to improve the correlation of 3T and 7T dictionaries based on the input 3T image. Also, we further incorporated group sparsity to share the sparsity among the neighboring 3T patches for reliable and accurate 7T MRI reconstruction. Such reconstruction was performed in a hierarchical patch-based approach to reconstruct the overall structure in the early stage and then the detailed structure in the final stages.

The experiments have been done based on the 3T and 7T MR images of 13 subjects. The results revealed that our method is able to recover more accurate structural details and has better numerical results than previous methods such as histogram-based method, sparse [25], CCA [41], MIMECS [35], LIS [38], and RF [36]. Additionally, the visual results support the superiority of our proposed method over the previous methods. Also, we evaluated the influence of post-processing methods such as brain tissue segmentation on the reconstructed 7T-like MR images. The results reveal that our reconstructed 7T-like images lead to higher accuracy in segmentation of WM, GM, CSF and skull, compared to segmentation of 3T MR images. In addition, we evaluate our proposed method for reconstruction of 7T-like images of patient with atrophy. The result reveals that in the reconstructed 7T-like image, the areas can be seen with higher resolution and contrast. Although in this paper we proposed a method for reconstruction of 7T-like MRI from 3T MRI, it can be also used for other MRI quality enhancements, such as estimation of 7T-like MRI from 1.5T MRI, or 3T-like MRI from 1.5T MRI.

Of note, if cortical lesions are not visible in the 3T MRI, it will be difficult to reconstruct them in the 7T-like MRI. However, it should be mentioned that, in the case of low-quality and low-contrast cortical lesions and atrophies in the 3T MRI, they can still be reconstructed with higher quality in the reconstructed 7T-like MRI. Also, another application of our proposed method is better segmentation of WM, GM and CSF from the reconstructed 7T-like MR images, compared to the original 3T MRI. Also, it is worth noting that the segmentation of small brain structures such as hippocampus subfields is generally difficult in the 3T MR images, while it is feasible in 7T MR images [43], [44]. Therefore, by reconstruction of 7T-like MR images from 3T MR images, better tissue segmentation can be achieved by using 7T-like images since 7T-like images are similar to the ground-truth 7T images in terms of image contrast and resolution.

Also, it should be mentioned that, to handle the applicability of our proposed method for different 3T MRI datasets, we use some pre-processing on the 3T MR images to make them have similar intensity ranges. For instance, we normalized all the images within the range of [0, 1]. Also, we used histogram matching between the input 3T image and all the training 3T images to ensure that all the images are in the similar intensity range and similar contrast range. In future work, we will apply our method to more other databases. We will release our algorithm, as well as the 3T and 7T MRI datasets, later in our software website (http://www.med.unc.edu/bric/idea-group/free-softwares).

Supplementary Material

Refer to Web version on PubMed Central for supplementary material.

Acknowledgments

This work was supported by NIH grants (EB006733, EB008374, EB009634, MH100217, AG041721, AG049371, AG042599).

References

1. Kolka AG, Hendriksea J, Zwanenburg JJM, Vissera F, Luijtena PR. Clinical applications of 7T MRI in the brain. Eur J Radiol. 82:708–718.
2. Beisteiner R, et al. Clinical fMRI: Evidence for a 7T benefit over 3T. Neuroimage. 2011; 57:1015–1021. [PubMed: 21620980]
3. DOTmed Daily News 2012.
4. Shi F, Cheng J, Wang L, Yap PT, Shen D. LRTV: MR image super-resolution with low-rank and total variation regularizations. IEEE Trans Med Imag. Dec; 2015 34(12):2459–2466.
5. Xu H, Zhai G, Yang X. Single image super-resolution with detail enhancement based on local fractal analysis of gradient. IEEE Trans Circuits Syst Video Technol. Oct; 2013 23(10):1740–1754.
6. Zhang K, Gao X, Tao D, Li X. Single image super-resolution with non-local means and steering kernel regression. IEEE Trans Image Process. Nov; 2012 21(11):4544–4556. [PubMed: 22829403]

7. Protter M, Elad M, Takeda H, Milanfar P. Generalizing the non-local-means to super-resolution reconstruction. IEEE Trans Image Process. Jan; 2009 18(1):36–51. [PubMed: 19095517]

8. Islam R, Lambert AJ, Pickering MR, Scarvell JM, Smith PN. A wavelet-based super-resolution method for multi-slice MRI. J Biomed Sci Eng. 2014; 5(12):862–870.

9. Plenge E, et al. Super-resolution methods in MRI: can they improve the trade-off between resolution, signal-to-noise ratio, and acquisition time? Magn Reson Med. 2012; 68(6):1983–1993. [PubMed: 22298247]

10. Shilling RZ, Robbie TQ, Bailloeul T, Mewes K, Mersereau RM, Brummer ME. A super-resolution framework for 3-D highresolution and high-contrast imaging using 2-D multislice MRI. IEEE Trans Med Imag. May; 2009 28(5):633–644.

11. Shi F, Cheng J, Wang L, Yap PT, Shen D. Longitudinal guided super-resolution reconstruction of neonatal brain MR images. Med Image Anal. 2013; 17:113–132. [PubMed: 23102924]

12. Shi F, Cheng J, Wang L, Yap PT, Shen D. LRTV: MR image super-resolution with low-rank and total variation regularizations. IEEE Trans Med Imag. Dec; 2015 34(12):2459–2466.

13. Woo J, et al. Super-resolution reconstruction for tongue MR images. Med Imag, Image Process. 2012; 8314:1–8.

14. Freeman WT, Jones TR, Pasztor EC. Example-based super resolution. IEEE Comput Graph Appl. 2002; 22(2):56–65.

15. Chan T-M, Zhang J, Pu J, Huang H. Neighbor embedding based super-resolution algorithm through edge detection and feature selection. Pattern Recog Lett. 2009; 30(5):494–502.

16. Yang J, Wang Z, Lin Z, Cohen S, Huang TS. Coupled dictionary learning for image super-resolution. IEEE Trans Image Process. Aug; 2012 21(8):3467–3478. [PubMed: 22481818]

17. Yang J, Lin Z, Cohen S. Fast image super-resolution based on in-place example regression. Proc CVPR. 2013:1059–1066.

18. Gao X, Zhang K, Tao D, Li X. Image super-resolution with sparse neighbor embedding. IEEE Trans Image Process. Jul; 2012 21(7):3194–3205. [PubMed: 22411005]

19. Yang MC, Wang YCF. A self-learning approach to single image super-resolution. IEEE Trans Multimedia. Apr; 2013 15(3):498–508.

20. Peleg T, Elad M. A statistical prediction model based on sparse representations for single image super-resolution. IEEE Trans Image Process. Jun; 2014 23(6):2569–2582. [PubMed: 24815620]

21. Jiang J, Hu R, Wang Z, Han Z. Face super-resolution via multilayer locality-constrained iterative neighbor embedding and intermediate dictionary learning. IEEE Trans Image Process. Oct; 2014 23(10):4220–4231. [PubMed: 25134081]

22. Dang CT, Aghagolzadeh M, Moghadam AA, Radha H. Single image super resolution via manifold linear approximation using sparse subspace clustering. Proc GlobalSIP. 2013:949–952.

23. Zhang K, Tao D, Gao X, Li X, Xiong Z. Learning multiple linear mappings for efficient single image super-resolution. IEEE Trans Image Process. Mar; 2015 24(3):846–861. [PubMed: 25576571]

24. Zhou F, Yuan T, Yang W, Liao Q. Single image super-resolution based on compact KPCA coding and kernel regression. IEEE Signal Process Lett. Mar; 2015 22(3):336–340.

25. Yang J, Wright J, Huang T, Ma Y. Image super-resolution via sparse representation. IEEE Trans Image Process. Nov; 2010 19(11):2861–2873. [PubMed: 20483687]

26. Mu G, Gao X, Zhang K, Li X, Tao D. Single image super resolution with high resolution dictionary. Proc IEEE Int Conf Image Process. 2011:1165–1168.

27. Dong W, Zhang L, Shi G, Wu X. Image deblurring and super-resolution by adaptive sparse domain selection and adaptive regularization. IEEE Trans Image Process. Jul; 2011 20(7):1838–1857. [PubMed: 21278019]

28. Kim KI, Kwon Y. Single-image super-resolution using sparse regression and natural image prior. IEEE Trans Pattern Anal Mach Intell. Jun; 2010 32(6):1127–1133. [PubMed: 20431136]

29. Gao X, Zhang K, Li X, Tao D. Joint learning for single-image super-resolution via a coupled constraint. IEEE Trans Image Process. Feb; 2012 21(2):469–480. [PubMed: 22262669]

30. Rueda A, Malpica N, Romero NE. Single-image super-resolution of brain MR images using overcomplete dictionaries. Med Image Anal. 2013; 17:113–132. [PubMed: 23102924]

31. Zhang Y, et al. Hierarchical patch-based sparse representation—A new approach for resolution enhancement of 4D-CT lung data. IEEE Trans Med Imag. Nov; 2012 31(11):1993–2005.
32. Bhavsar A, Wu G, Lian J, Shen D. Resolution enhancement of lung 4D-CT via group-sparsity. Med Phys. 2013; 40(12):121717:1–14. [PubMed: 24320503]
33. Manjon JV, Coupe P, Buades A, Collins DL, Robles M. MRI super-resolution using self-similarity and image priors. Int J Biomed Imag. 2010:1–12.
34. Coupe P, Manjon JV, Chamberland M, Descoteaux M, Hiba B. Collaborative patch-based super-resolution for diffusion-weighted images. Med Phys. 2013; 10:245–61.
35. Roy S, Carass A, Prince JL. Magnetic resonance image example based contrast synthesis. IEEE Trans Med Imag. Dec; 2013 32(12):2348–2363.
36. Huynh T, et al. Estimating CT image from MRI data using structured random forest and auto-context model. IEEE Trans Med Imag. Jan; 2015 35(1):174–183.
37. Alexander DC, Zikic D, Zhang J, Zhang H, Criminisi A. Image quality transfer via random forest regression: Applications in diffusion MRI. Proc MICCAI. 2014:225–232.
38. Burgos N, et al. Attenuation correction synthesis for hybrid PET-MR scanners: Application to brain studies. IEEE Trans Med Imag. Dec; 2014 33(12):2332–2341.
39. Burgos N, et al. Multi-contrast attenuation map synthesis for PET/MR scanners: Assessment on FDG and florbetapir PET tracers. Eur J Nucl Med Mol Imag. 2015; 42(9)
40. Ashburner J, Friston KJ. Unified segmentation. Neuroimage. 2005; 29:839–851.
41. Huang H, He H, Fan X, Zhang J. Super-resolution of human face image using canonical correlation analysis. Pattern Recognit. 2010; 43:2532–2543.
42. Bahrami K, et al. Hierarchical reconstruction of 7T-like images from 3T MRI using multi-level CCA and group sparsity. Proc MICCAI. 2015:659–666.
43. Leemput KV, et al. Automated segmentation of hippocampal subfields from ultra-high resolution in vivo MRI. Neuroscience. 2009; 19:549–557.
44. Wissea LEM, et al. Subfields of the hippocampal formation at 7 T MRI: In vivo volumetric assessment. Neuroimage. 2012; 61:1043–1049. [PubMed: 22440643]
45. Hertzmann A, Jacobs CE, Oliver N, Curless B, Salesin DH. Image analogies. SIGGRAPH 01. 2001
46. Holmes CJ, Hoge R, Collins L, Woods R, Toga AW. Enhancement of MR images using registration for signal averaging. J Comput Assist Tomogr. 1998; 22:324–333. [PubMed: 9530404]
47. Shi F, et al. LABEL: Pediatric brain extraction using learning-based meta-algorithm. Neuroimage. 2012; 62(3):1975–1986. [PubMed: 22634859]

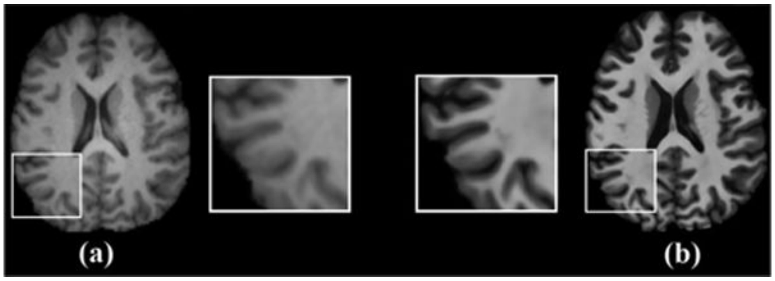

Fig. 1.
Axial views of (a) 3T MRI and (b) 7T MRI of the same subject, together with the zoomed regions. 7T MRI shows better anatomical details and tissue contrast compared to 3T MRI.

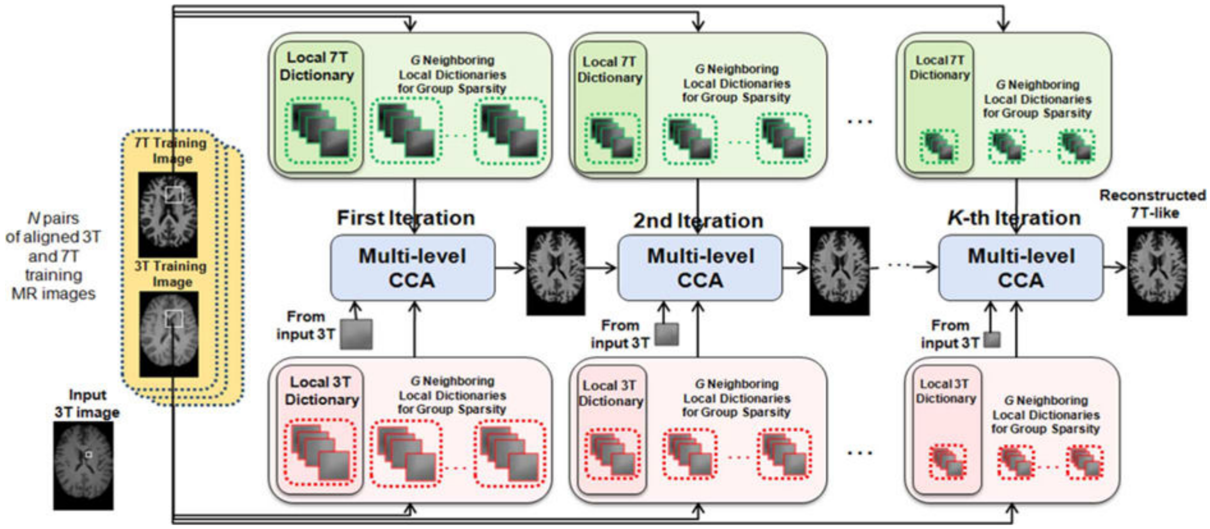

Fig. 2.

Proposed framework for the reconstruction of 7T-like MRI from 3T MRI.

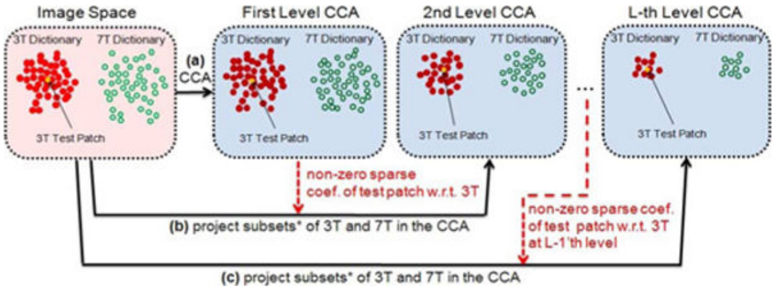

Fig. 3.

Illustration of multi-level CCA. (a) CCA, (b) 2nd level CCA, and (c) *L*-th level CCA. *The 3T and 7T subsets in image space are indicated based on non-zero sparse coefficients of test patch with respect to 3T dictionary at the previous level.

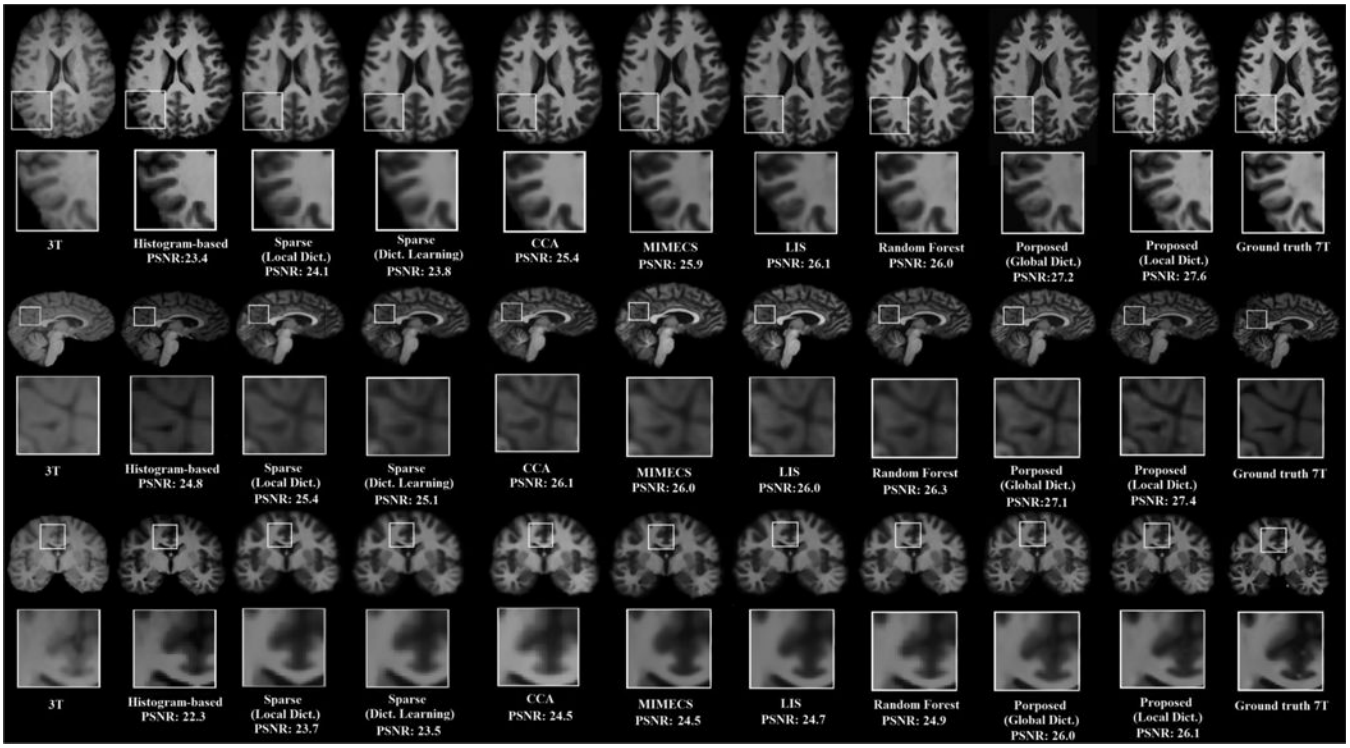

Fig. 4.

Visual comparison of axial, sagittal and coronal views of reconstructed 7T-like images from top to bottom rows, together with close-up view of specific region. From top to bottom, the axial, sagittal and coronal views are shown. From left to right columns: 3T image, reconstructed results by histogram-based method, sparse [25] (local dict.), sparse [25] (dict. learning), CCA [41], MIMECS [35], LIS [38], RF [36], our method with local dictionary, and our method with global dictionary, as well as ground-truth 7T MRI.

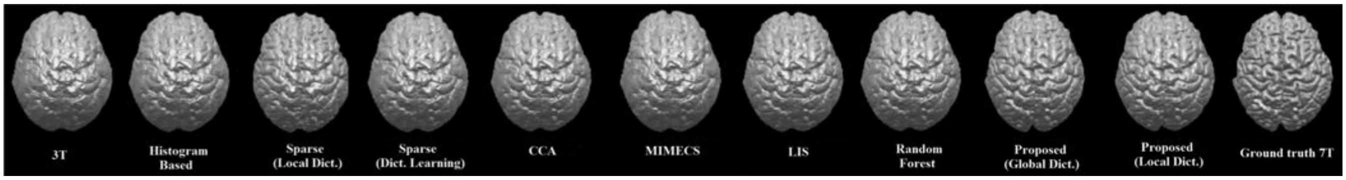

Fig. 5.
From left to right: visual comparison of cortical surface rendering of 3T image, reconstructed 7T-like images by histogram-based method, sparse [25] (local dict.), sparse [25] (dict. learning), CCA [41], MIMECS [35], LIS [38], RF [36], our method with local dictionary, and our method with global dictionary, as well as ground-truth 7T MRI.

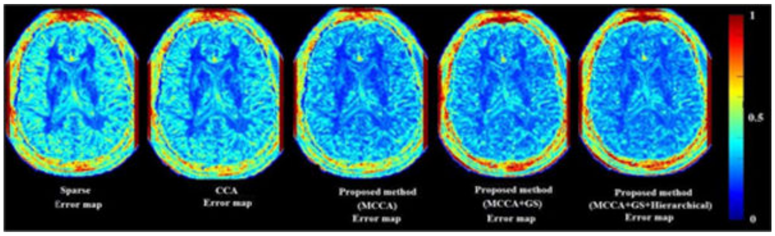

Fig. 6.

Evaluation of error maps of axial view of intermediate results of our proposed method. From left to right columns: reconstructed image based on sparse representation [25], reconstructed image based on CCA [41], outputs of ‘MCCA’, ‘MCCA + GS’ and ‘MCCA + GS+ Hierarchical’ steps of our proposed method.

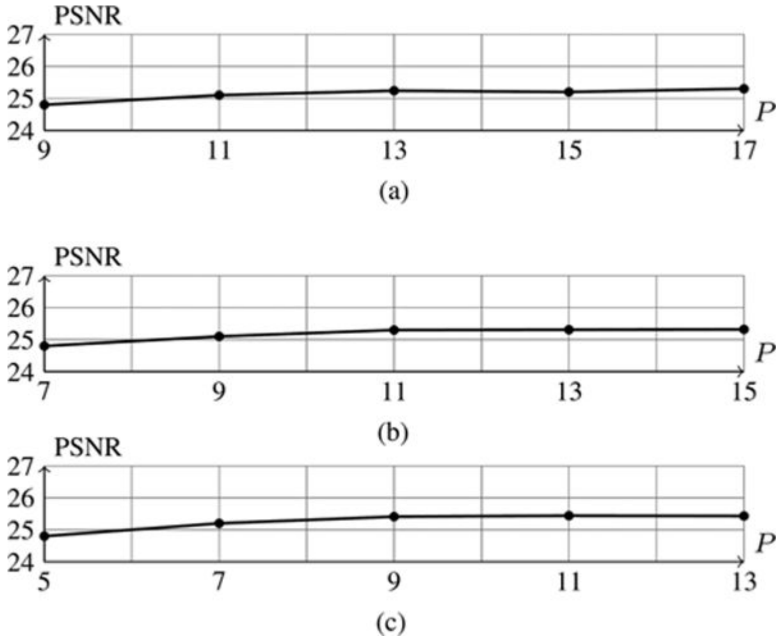

Fig. 7.

Mean performance (PSNR) of our proposed method at three iterations for different search window size (*P*) for all subjects. (a) 1’st iteration (b) 2’nd iteration (c) 3’rd iteration.

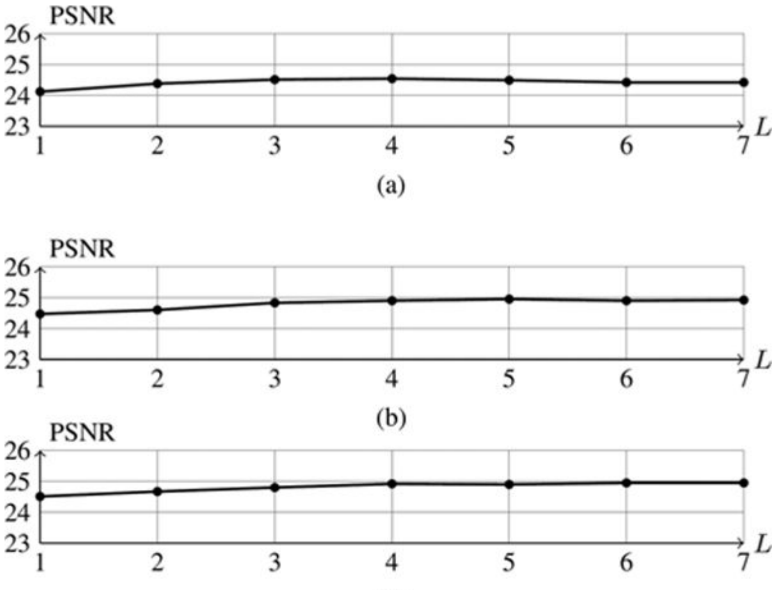

(a) (b) (c)

Fig. 8.

Mean performance (PSNR) of our proposed method at three iterations in terms of number of levels in the multi-level CCA for all subjects. (a) 1’st iteration (b) 2’nd iteration (c) 3’rd iteration.

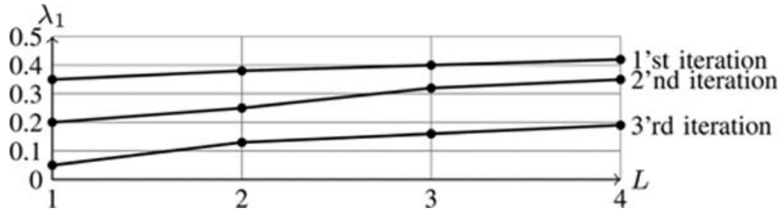

Fig. 9.

The best sparsity parameters λ_1 for each level L in multi-level CCA and each iteration in hierarchical reconstruction.

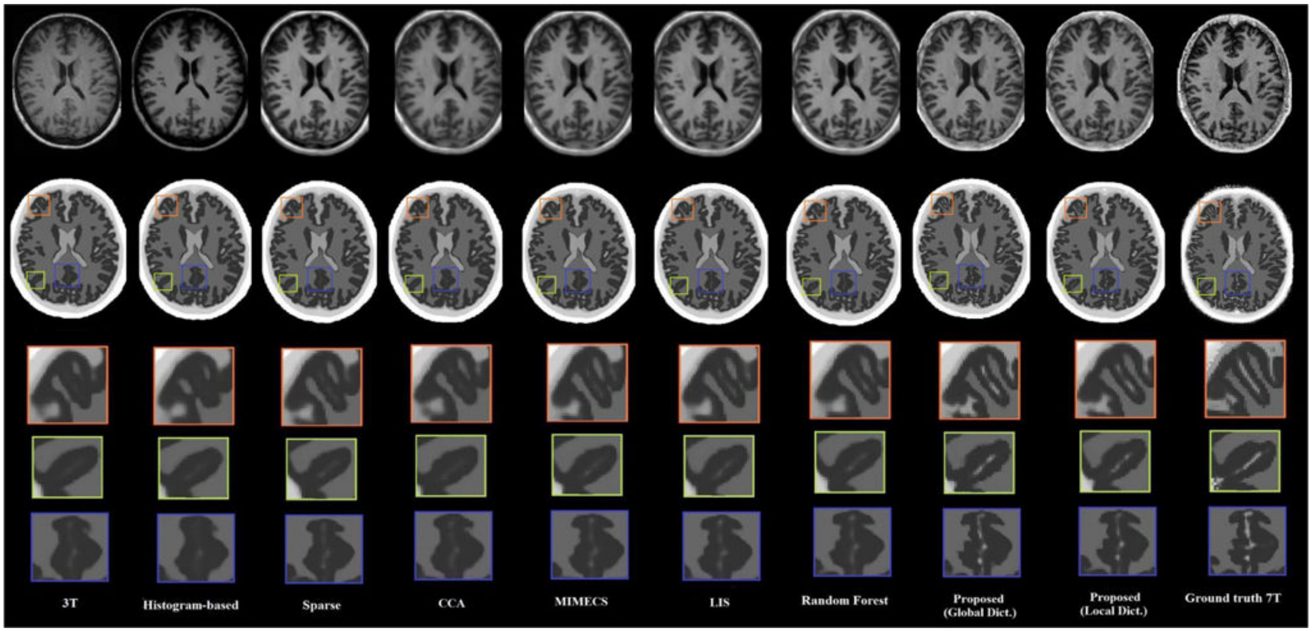

Fig. 10.
Comparison of tissue segmentation results by different methods. From left to right: axial view of a subject together with segmentation results and close-up views of selected regions for 3T MRI and the reconstructed 7T-like MRI data by histogram-based method, sparse representation [25], CCA [41], MIMECS [35], LIS [38], RF [36], our method with local dictionary, and our method with global dictionary, and ground-truth 7T MRI.

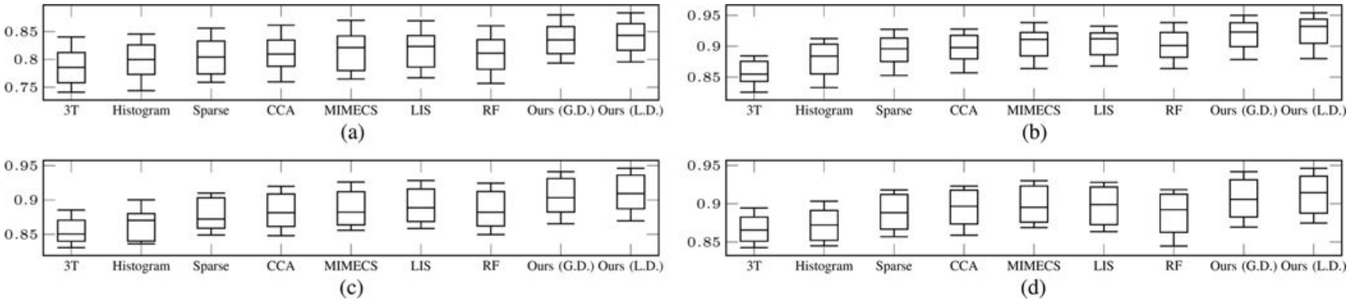

Fig. 11.

Box plot of the Dice ratio for segmentation of (a) GM, (b) WM, (c) CSF and (d) skull by different methods. From left to right: 3T MRI and the 7T-like images by histogram-based method, sparse representation [25], CCA [41], MIMECS [35], LIS [38], RF [36], our method with local dictionary (Ours (L.D.)), and our method with global dictionary (Ours (G.D.)), respectively.

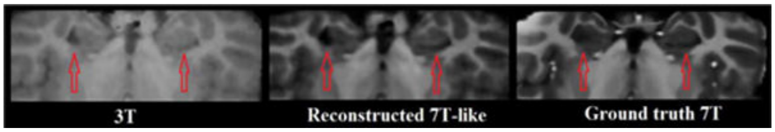

Fig. 12.

Illustration of reconstruction results for a brain region of one patient with two atrophies close to right and left hippocampus areas. From left to right columns: 3T, reconstructed 7T-like, and ground-truth 7T MRI.

TABLE I

Performance Comparison of the Methods in Terms of PSNR, VIF, UQI and SSIM

(a)

Method	Hist. based	Sparse (Local Dict.) Yang *et al.* 2010	Sparse (Dict. Learning) Yang *et al.* 2010	CCA Huang *et al.* 2010	MIMECS Roy *et al.* 2013	LIS Burgos *et al.* 2014	RF Huynh *et al.* 2015	Proposed (Global Dict.)	Proposed (Local Dict.)
Average	20.8	23.0	22.4	23.5	23.8	23.9	23.7	**24.8**	**25.0**
Std. Dev.	1.42	1.19	1.25	1.02	1.22	1.24	1.21	1.16	**1.18**

(b)

Method	Hist. based	Sparse (Local Diet) Yang *et al.* 2010	Sparse (Dict. Learning) Yang *et al.* 2010	CCA Huang *et al.* 2010	MIMECS Roy *et al.* 2013	LIS Burgos *et al.* 2014	RF Huynh *et al.* 2015	Proposed (Global Dict.)	Proposed (Local Dict.)
Average	0.27	0.30	0.31	0.33	0.35	0.35	0.34	**0.40**	**0.42**
Std. Dev.	0.043	0.052	0.062	0.041	0.032	0.043	0.045	0.035	0.032

(c)

Method	Hist. based	Sparse (Local Diet) Yang *et al.* 2010	Sparse (Dict. Learning) Yang *et al.* 2010	CCA Huang *et al.* 2010	MIMECS Roy *et al.* 2013	LIS Burgos *et al.* 2014	RF Huynh *et al.* 2015	Proposed (Global Dict.)	Proposed (Local Dict.)
Average	0.26	0.32	0.34	0.34	0.41	0.40	0.39	**0.44**	**0.46**
Std. Dev.	0.053	0.045	0.035	0.046	0.047	0.052	0.051	0.045	0.042

(d)

Method	Hist. based	Sparse (Local Diet) Yang *et al.* 2010	Sparse (Dict. Learning) Yang *et al.* 2010	CCA Huang *et al.* 2010	MIMECS Roy *et al.* 2013	LIS Burgos *et al.* 2014	RF Huynh *et al.* 2015	Proposed (Global Dict.)	Proposed (Local Dict.)
Average	0.30	0.30	0.32	0.35	0.36	0.40	0.38	**0.48**	**0.47**
Std. Dev.	0.055	0.055	0.033	0.041	0.031	0.045	0.046	0.048	0.044

TABLE II

P-Values by Performing Permutation Test Between our Proposed Method and all the Previous Methods for PSNR, VIF, UQI, and SSIM Values

Method	**Hist based**	**Sparse (Local Dict.)**	**Sparse (Dict. Learning)**	**CCA**	**MIMECS**	**LIS**	**RF**
PSNR	0.0001	0.0002	0.0002	0.0002	0.0040	0.0040	0.0040
VIF	0.0001	0.0001	0.0001	0.0001	0.0002	0.0002	0.0001
UQI	0.0001	0.0001	0.0001	0.0001	0.0004	0.0004	0.0002
SSIM	0.0001	0.0001	0.0001	0.0001	0.0002	0.0002	0.0002

TABLE III

Performance Comparison of Our Proposed Method and Patch Similarity-Based CCA When 100%, 80%, 60%, 40%, 20%, and 10% of the Most Similar Patches in the Neighborhood Search Window are Used to Build the Local 3T and 7T Dictionaries, Respectively

Methods	**Patch Similarity-based CCA**						**Proposed method**
Local Dictionary Size (% of neighborhood patches)	**100%**	**80%**	**60%**	**40%**	**20%**	**10%**	**–**
Mean PSNR	23.5	23.5	23.6	23.9	24.0	24.0	25.0
Std. Dev. of PSNR	1.32	1.24	1.36	1.21	1.22	1.15	1.18

TABLE IV

The Number of Patches in the Local Dictionary (% of Total Patches in the Local Dictionary) Which Have Non-Zero Coefficients in λ_1 at Each Level of Three Iterations

Iteration	Local Dictionary Size	level 1 (%)	level 2 (%)	level 3 (%)	level 4 (%)
1	26364	6850 (26%)	1580 (23%)	350 (22%)	65 (19%)
2	15972	4470 (28%)	1118 (25%)	257 (23%)	50 (19%)
3	8748	2620 (30%)	680 (26%)	150 (22%)	30 (20%)